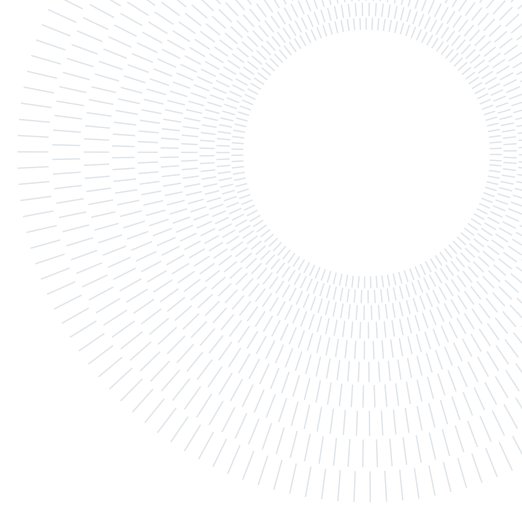




**POLITECNICO**  
MILANO 1863

SCUOLA DI INGEGNERIA INDUSTRIALE  
E DELL'INFORMAZIONE



# Aeroacoustic computation based on the Harmonic Balance method in SU2

TESI DI LAUREA MAGISTRALE IN  
AERONAUTICAL ENGINEERING - INGEGNERIA AERONAUTICA

JASIM JAMIL, 10586811

**Advisor:**  
Prof. Alberto Guardone

**Co-advisors:**  
Dr. Luca Abergio

**Academic year:**  
2022-2023

**Abstract:** This paper presents the application of a reduced order model called Harmonic Balance method (HB) to perform aerodynamic and aeroacoustic analysis of quasi-periodic external flows. The time spectral method was already implemented in the open-source PDE solver SU2 and in this work is applied in the field of aeroacoustic prediction. A uniform time sampling inside the dominant period is adopted and the solution is found for  $2K+1$  time instances, where  $K$  is the number of solved frequencies. The computational cost is strongly reduced with respect to a fully time-accurate unsteady Reynolds-Averaged Navier-Stokes (URANS) simulation. To obtain a more time-resolved solution necessary for acoustic prediction, spectral interpolation has been implemented to interpolate the solution for an arbitrary number of instances inside a specified time range. In a modular style, the surface solution is used by the computational aeroacoustic (CAA) module, implemented in SU2, which uses Farassat's 1A formulation to compute the pressure perturbation perceived by far-field observers for tonal noise prediction. Finally, the aerodynamic and aeroacoustic results obtained with the proposed framework are compared with time-accurate solutions using three test cases.

**Key-words:** HARMONIC BALANCE, SPECTRAL INTERPOLATION, SU2, FARASSAT 1A FORMULATION,  $O_{pt}TP$  ALGORITHM, UNSTEADY SIMULATION

## 1. Introduction

The field of Computational Fluid Dynamics (CFD) has witnessed notable advancements in predicting complex, unsteady flows. However, accurately simulating unsteady flows, particularly in aeronautical applications, poses a significant challenge due to the substantial computational time and resource requirements. Traditional methods like Direct Numerical Simulation (DNS) and Large-Eddy Simulation (LES) [1, 2] provide high precision but demand extensive computational resources and time. In these simulations, a substantial portion of initial iterations is dedicated to resolving the transient phase, which, in practice, offers limited practical value[3]. Moreover, conventional design optimization has predominantly concentrated on steady-state flow physics [4]. The integration of unsteady aerodynamics into design procedures has the potential to shape next-generation aerospace vehicles with enhanced efficiency, reduced fuel consumption, and lower noise emissions. Emphasizing the significance of unsteady flow computation, it is crucial to consider various aeronautical scenarios such as Urban Air Mobility [5], which has garnered substantial interest as a solution to traffic congestion in densely populated regions, as well as applications in wind turbines [6], jet engines[7], and turbo-machines[8]. Therefore,

there is an urgent need to develop cost-effective techniques that strike a balance between accuracy and computational cost. In recent times, alongside the pursuit of aerodynamically efficient designs, there has been a growing demand for predicting, analyzing, and mitigating the noise generated by aircraft. This is particularly relevant for rotary aircraft, such as Vertical Take-Off and Landing (VTOL) aircraft like drones and helicopters, and rotary wing components like rotors, propellers, and engines[9]. The urgency in addressing aircraft noise has been further heightened by increasingly stringent aviation noise regulations, emphasizing the quest for quieter design solutions[10]. In response to this challenge, Computational Aero-Acoustic (CAA) codes have been developed to calculate and analyze noise emissions. These codes rely on unsteady CFD solutions as input data for aeroacoustic noise propagation, further motivating the exploration of efficient and accurate computational techniques for solving unsteady flows[11]. The importance of these advancements is particularly underscored in the context of helicopter operations and the emerging field of Urban Air Mobility, where unsteady flow considerations play a pivotal role in achieving optimal performance and meeting regulatory requirements.

In this work, a reduced-order model known as the Harmonic Balance method (HB)[12] which falls under the category of numerical methods referred to as time spectral methods, is presented and investigated. Harmonic Balance method presents a significant advantage in terms of computational efficiency compared to conventional time-accurate methods by eliminating the need to compute the transient phase of the simulation. This is achieved by employing a Fourier representation in time of the conservative variables and by directly computing the periodic solution at regime, thus bypassing the requirement to resolve numerical transients[13]. By solving the complete nonlinear unsteady Reynolds-Averaged Navier-Stokes (URANS) equations, this method can accurately capture all unsteady effects, provided that an adequate number of frequencies are included. Notably, what sets harmonic balance apart from other time spectral methods is that the specific set of frequencies does not necessarily have to be integral multiples of each other[14, 15].

The solution obtained through Harmonic Balance consists of conservative variables computed at specific time instances inside the assigned period. In this study, a uniform time sampling approach[16] is adopted to discretize the time domain. As a result, the solution is accessible only in  $N$  instances, where  $N$  corresponds to  $2K+1$  instances and  $K$  denotes the number of user-specified input frequencies. Consequently, to facilitate post-processing and later aeroacoustic noise analysis, it becomes imperative to increase the resolution of the solution in time. Therefore, this study also presents spectral interpolation[17] and its implementation to interpolate the solution for an arbitrary duration with an arbitrary number of time instances.

Unfortunately, the harmonic balance method with uniform sampling of the time domain has been known to have stability issues for certain sets of frequencies. Extensive investigations into this issue have led to a range of solutions proposed in existing literature[18]. These solutions span from oversampling the time domain to using non-uniform time sampling, and many other complex methods like gradient-based OPTimization (OPT) algorithm[19]. This study introduces and implements a uniform time sampling algorithm named the Optimal Time Period (OptTP) algorithm[14]. This algorithm is not only simple to implement compared to alternative methods but also delivers performance comparable to the robustness observed in the OPT algorithm, which has proven to be the most robust choice up to this point.

Once the solution of the flow field has been obtained with the Harmonic Balance method, an aeroacoustic noise analysis is performed to assess its noise-predicting capabilities. In recent years, there has been an increase in faster and more robust predicting codes to perform aeroacoustic noise prediction. Historically, a series of theories based on the acoustic analogy, in particular, Lighthill's acoustic analogy[20, 21] have been used as a main tool for predicting aeroacoustic noise. In this approach, the Navier-Stokes equations are transformed into a non-homogeneous wave equation and all the remaining terms are grouped into a source term defined as Lighthill's stress tensor. Later, Lighthill's acoustic analogy approach was extended by including the effects of arbitrary types of surfaces in arbitrary motions and the so-called Ffowcs Williams and Hawkings (FW-H) equation was derived[22]. Using the mathematical theory of generalized functions, the Navier-Stokes equations are rearranged into a non-homogeneous wave equation with two surface source terms and one volume source term. The two surface source terms are known as monopole or thickness source term, which models the noise generated by the displacement of fluid as the body moves, and the dipole or loading source term, which models the noise that results from the unsteady motion of the pressure distribution on the body. The volume source term, also known as the quadrupole source term, models the non-linearities due to both the local sound speed variation and the finite fluid velocity near the body. However, the quadrupole source term is often neglected because of the high computational demand for determining the flow field with sufficient accuracy and the high cost of volume integration. Moreover, when dealing with subsonic flow fields, the acoustic noise perceived by observers which are usually placed far from the noise sources, predominantly consists of tonal noise which is composed of thickness noise and loading noise[23].

In this investigation, to propagate the noise from the emitter to an observer location, an integral method based on Farassat’s 1A formulation is employed which exploits the free-space Green’s function for the FW-H equation. This results in an integral formulation that is solved numerically by providing the input data as the flow field solution in the nearfield region[24]. This approach has the distinct advantage of eliminating the need for calculating time derivatives, and solely surface integrals on the body need to be solved, which only requires the solution from CFD computation on the surface of the body as input.

All the CFD simulations and aeroacoustic analysis were performed using the SU2-suite[25–27], which is an open-source collection of tools for the analysis of partial differential equations (PDEs) and PDE-constrained optimization problems on unstructured meshes with state-of-the-art numerical methods as it already contains the implementation of Harmonic balance and a CAA module based on the Farassat’s 1A formulation[28]. To assess the accuracy of the solution obtained through Harmonic Balance and its subsequent aeroacoustic noise propagation, the results were confronted with the time-accurate solution using three test cases which consists of a 2D NACA64A10 pitching airfoil, a 3D NACA6410 pitching rectangular wing and a rigid isolated propeller immersed in a uniform flow.

In section 2, an exposition of the mathematical formulation and the implementation of Harmonic Balance method (HB), Farassat’s 1A formulation for Ffowcs Williams and Hawkings (FW-H) equation and spectral interpolation for Harmonic Balance is presented. In section 3, a brief introduction to stability analysis to identify possible causes of instability in the Harmonic Balance method is performed with the implementation of the OptTP algorithm to solve these stability issues. Section 4 presents the results obtained from the Harmonic Balance method and the time-accurate simulation together with the aeroacoustic noise propagation. Finally, the conclusions drawn from this study have been presented in section 5.

## 2. Numerical Methods

In this section, an overview of the governing flow equations, the Harmonic Balance method, Farassat’s 1A formulation for Ffowcs Williams-Hawkings equations and spectral interpolation are presented along with their implementation in SU2.

### 2.1. Governing equations

In SU2, the unsteady compressible Navier-Stokes equations in semi-discretized form are obtained using a Finite Volume Method (FVM) and after spatial integration over a control volume and time discretization, these equations can be expressed as

$$\mathbf{D}_t \mathbf{U} |\Omega| + \mathbf{R}(\mathbf{U}) = 0 \quad (1)$$

Here,  $\mathbf{U}$  represents the vector of conservative variables, and  $|\Omega|$  represents the control volume. The residual,  $\mathbf{R}(\mathbf{U})$ , encompasses convective and viscous fluxes integrated over the surface area of a cell, as well as any source terms integrated within the cell’s volume. The operator  $\mathbf{D}_t$  denotes the partial derivative operator with respect to time, which can be approximated with any time discretizing schemes like explicit or implicit finite difference method for time-accurate methods. A dual time-stepping method is used for time integration by solving each physical time step as a steady-state problem in pseudo-time  $\tau$  [29].

$$|\Omega| \frac{\partial U_n}{\partial \tau} + |\Omega| \mathbf{D}_t U_n + \mathbf{R}(U_n) = |\Omega| \frac{\partial U_n}{\partial \tau} + \mathbf{R}^*(U_n) = 0 \quad (2)$$

In order to solve the pseudo-time integration, an implicit first-order backward difference scheme is employed. But for implicit integration, it is necessary to linearize the residual and construct the Jacobian for each time instance. A first-order linearization of the residual  $\mathbf{R}(\mathbf{U})^*$  is adopted with respect to the physical time step,  $n$ . Consequently, the final resulting linear system to be solved for the flow state  $U_n^{q+1}$  for pseudo-time step  $q + 1$  can be expressed as follows:

$$U_n^{q+1} - U_n^q + \frac{\Delta \tau}{|\Omega|} \left( \mathbf{R}^*(U_n^q) + \frac{\partial \mathbf{R}^*(U_n^q)}{\partial U_n} \cdot (U_n^{q+1} - U_n^q) \right) = 0 \quad (3)$$

### 2.2. Harmonic Balance method

The Harmonic Balance (HB) method was implemented in SU2 by [15]. Here a brief theory for Harmonic Balance method and its implementation is presented. The primary difference between a time-accurate scheme

and Harmonic Balance is the definition of the partial derivative operator,  $\mathbf{D}_t$  defined in equation 1. Let's consider a scalar variable  $\phi$  defined within a control volume, denoted by the superscripts ' $*$ ' and ' $\wedge$ ' to represent it in the time and frequency domain, respectively. The time period  $T$  is divided into  $N$  time instances. Throughout this paper, uniform time-sampling of the time domain is adopted and the resulting instances  $t_n$  are  $t_n = (n-1)T/N$ , where  $n$  goes from 0 to  $N-1$ . The set of input frequency vector is represented by  $\underline{\omega} = [\omega_0, \omega_1, \dots, \omega_K, \omega_{-K}, \dots, \omega_{-1}]^T$  and  $\omega_{-K} = -\omega_K$  because the flow variables are real and the operator matrix has to be real. In this analysis, the time period  $T$  is chosen to be  $T = 2\pi/\omega_{min}$  and  $\omega_{min}$  corresponds to the minimum frequency from the set of input frequencies  $\underline{\omega}$ . The value  $K$  represents the number of input frequencies and is related to the number of time instances  $N$ [14] by:

$$N = 2K + 1 \quad (4)$$

The vector  $\phi^*$  consists of a conservative variable  $\phi$  evaluated at each time instance, i.e.  $\phi^* = [\phi_0, \phi_1, \dots, \phi_{N-1}]^T$ . This vector,  $\phi^*$  is transformed into  $\hat{\phi}$ , the vector of Fourier coefficients in the frequency domain, denoted as  $\hat{\phi} = [\hat{\phi}_0, \hat{\phi}_1, \dots, \hat{\phi}_K, \hat{\phi}_{-K}, \dots, \hat{\phi}_{-1}]^T$ , using a Discrete Fourier Transform (DFT) matrix, denoted by  $E$  using the following relation,

$$\hat{\phi} = E\phi^* \quad (5)$$

where,

$$E_{(k,n)} = \frac{1}{N} e^{-i\omega_k t_n} \quad (6)$$

$$\hat{\phi}_k = \frac{1}{N} \sum_{n=0}^{N-1} \phi_n e^{-i\omega_k t_n} \quad (7)$$

By utilizing the definitions provided in Equation 5 and recognizing that  $\hat{\phi}$  is a vector in the frequency domain and thus independent of time, the time derivative can be reformulated as follows:

$$D_t \phi^* = D_t (E^{-1} \hat{\phi}) = (D_t E^{-1}) \hat{\phi} = \frac{\partial E^{-1}}{\partial t} E \phi^* \quad (8)$$

Unfortunately, in the Harmonic Balance method, the frequencies doesn't necessarily have to be integral multiples of each other. As a result, an analytic formulation for the inverse of matrix  $E$  or called Inverse discrete Fourier Transform (IDFT) matrix,  $E^{-1}$ , does not exist. Therefore, it needs to be computed numerically by inverting the matrix  $E$ . Once the partial derivative is defined, as discussed before, the partial derivative operator matrix,  $\mathbf{D}_t$ , is used in the computation of the source term and added to the residual of corresponding governing equations in each control volume and then the  $N$  steady-state problems are simultaneously marched towards steady-state solution in pseudo-time.

### 2.3. Ffowcs Williams and Hawkings equation and Farassat's 1A formulation

The Ffowcs Williams and Hawkings equation (Equation 9) represents an alternative formulation of the conservation laws. In this form, the equation encompasses all types of noise components that are associated to distinct sources of aerodynamic noise, namely the monopole, dipole, and quadrupole terms.

$$\frac{1}{c^2} \frac{\partial^2 p'}{\partial t^2} - \nabla^2 p' = \frac{\partial}{\partial t} [\rho_0 v_n \delta(f)] - \frac{\partial}{\partial x_i} [p n_i \delta(f)] + \frac{\partial^2}{\partial x_i \partial x_j} [H(f) T_{ij}] \quad (9)$$

where  $p'$  is acoustic pressure,  $n_i$  is the unit outward normal,  $f = 0$  represents a moving control surface.  $\delta(f)$  and  $H(f)$  are the Dirac delta and Heaviside functions, respectively. Lastly,  $\rho_0$ ,  $v_n$ ,  $p$  and  $T_{ij}$  are defined as freestream density, normal surface velocity, the static pressure and Lighthill stress tensor, respectively. Farassat introduced a series of more practical integral formulations for the Ffowcs Williams and Hawkings (FW-H) equation[22]. In this work, Farassat's 1A formulation is used as it is already implemented in SU2[24]. In this formulation, the quadrupole term is neglected and so the acoustic noise is mainly tonal noise which is composed of thickness noise and loading noise.

$$p'(x, t) = p'_T(x, t) + p'_L(x, t) \quad (10)$$

Furthermore, all the time derivatives in the solution for the FW-H equation have been transformed into surface integrals on the body, which has the advantage of increasing the speed and accuracy of the CAA numerical code

and in addition, the computational time becomes independent of the observer distance. So the final solution for the acoustic pressure,  $p'$  is given as,

$$p'_T(\mathbf{x}, t) = \frac{1}{4\pi} \int_s \left[ \frac{\rho_0(\dot{U}_i n_i + U_i \dot{n}_i)}{r(1 - M_r)^2} \right]_{ret} dS + \frac{1}{4\pi} \int_s \left[ \frac{\rho_0 U_i n_i K}{r^2(1 - M_r)^3} \right]_{ret} dS \quad (11)$$

$$p'_L(\mathbf{x}, t) = \frac{1}{4\pi} \frac{1}{c} \int_s \left[ \frac{\dot{F}_i \hat{r}_i}{r(1 - M_r)^2} \right]_{ret} dS + \frac{1}{4\pi} \int_s \left[ \frac{F_i \hat{r}_i - F_i M_i}{r^2(1 - M_r)^2} \right]_{ret} dS + \frac{1}{4\pi} \frac{1}{c} \int_s \left[ \frac{F_i \hat{r}_i K}{r^2(1 - M_r)^3} \right]_{ret} dS \quad (12)$$

Where, for an impermeable surface

$$U_i = v_i \quad (13)$$

$$F_i = L_{ij} \mathbf{n}_j \quad (14)$$

$$\mathbf{L}ij = \mathbf{P}'_{ij} = (p - p_\infty) \delta_{ij} \quad (15)$$

$$K = \dot{M}_i \hat{r}_i \hat{r} + M_r c - M^2 c \quad (16)$$

$$M_r = \frac{v_i \hat{r}_i}{c} \quad (17)$$

and  $r$  is the radiation vector or distance between the observer and source points,  $\hat{r}_i$  represents the unit radiation vector.  $\dot{M}_i$  is the time derivative of the local Mach number,  $M$  which depends on the speed of sound,  $c$ , and local velocity,  $v_i$ . Lastly,  $dS$ ,  $\delta_{ij}$  and  $p_\infty$  are the local panel area, the Kronecker delta function and the freestream pressure respectively.

## 2.4. Spectral interpolation for Harmonic Balance method

As discussed in section 2.1, the solution obtained in time domain from Harmonic Balance method is inherently limited in terms of number of time instances. In this work, a uniform time-sampling of time domain is adopted and for a given number of input frequencies,  $K$ , the solution is found only for  $N$  time instances, where

$$N = 2K + 1 \quad (18)$$

To achieve a better time resolution of the flow solution with an arbitrary number of time instances and of arbitrary duration which can be utilized for post-processing or in this work mainly for aeroacoustic propagation, spectral interpolation is employed. Spectral interpolation is used because the solution is composed of harmonics whose frequencies are known and the solution for  $N$  time instances is also known [17]. So, the solution can be easily interpolated for any instance in time through the following procedure:

1. Given a vector of conservative variables obtained from Harmonic Balance,  $\phi^*$ , it is transformed into Fourier coefficients in the frequency domain using the DFT matrix,  $E$ . However, as there is no analytical formulation for  $E$ , the IDFT matrix,  $E^{-1}$ , is exploited using the following expression,

$$\hat{\phi} = (E^{-1})^{-1} \phi^* \quad (19)$$

where  $\hat{\phi}$  represents the vector containing the Fourier coefficients.

2. These Fourier coefficients are again transformed back into the time domain but instead of using the the original IDFT matrix, a larger interpolating IDFT matrix,  $E^{*-1}$  of size  $N^* \times N$  is used. In the place of the original time instances vector  $t$  used in the Harmonic Balance simulation, a different vector of time instances,  $t^*$  of length  $N^*$  greater than  $N$ , is used for interpolation which is defined by the user.

$$\phi = E^{*-1} \hat{\phi} \quad (20)$$

where  $\phi$  is the vector containing interpolated solution and  $E^{*-1}$  is defined as  $E_{n,k}^{*-1} = e^{i\omega_k t_n^*}$ .

Through this procedure, all the conservative variables and integral quantities like lift coefficient and drag coefficient are interpolated. For other kinematic and geometric quantities such as surface normals and grid velocity vectors, built-in functions available in the SU2 code were modified and then employed to find their corresponding values for user-defined time instances vector  $t^*$ .

### 3. Stability analysis

It has been observed that Harmonic Balance method exhibits unreliability when dealing with specific sets of frequency, leading to instability and in certain cases divergence of the simulation. In this section, the underlying cause of this instability issue is presented and analyzed, followed by a possible solution along with its implementation in SU2.

#### 3.1. IDFT matrix

It has been observed that the high condition number of the inverse Discrete Fourier Transform (IDFT) matrix  $E^{-1}$ , is the primary factor responsible for stability issues present in Harmonic Balance method[30]. By definition, for a linear system,

$$Ax = b \quad (21)$$

the quantification of the amplification of errors in input vector  $x$ , is determined by the condition number of matrix  $A$ ,  $\kappa(A)$  through the following expression,

$$\frac{\|x - \tilde{x}\|}{\|x\|} \leq \kappa(A) \frac{\|A - \tilde{A}\|}{\|A\|} \quad (22)$$

Larger condition number result in a greater amplification of the input, which can lead to system instability. Therefore, in the case of the Harmonic Balance method, the extent of error amplification is governed by the condition number of the operator matrix  $D_t$ , which is composed of IDFT matrix which is inherently ill-conditioned. When the full spectrum of the actual flow problem is truncated to a limited number of discrete frequencies provided as input to Harmonic Balance method, aliasing errors arise during the conversion between the time and frequency domains of the conservative variables through  $E^{-1}$  matrix[31]. As the condition number of  $E^{-1}$  matrix increases, larger errors are introduced into the system due to higher amplification. Given that the system matrix  $D_t$  is inherently ill-conditioned, small increments of errors even at low condition number of 10 (a heuristic approximation based on numerical simulations) can be significant enough to make the simulation diverge. Moreover, when the frequencies are arbitrary, it is generally challenging to select a uniformly spaced set of time instances where the IDFT matrix is well-conditioned. In fact, it is common for uniformly sampled sinusoids at multiple frequencies to exhibit a near-linear dependence, resulting in them being non-orthogonal and thus contributing to the ill-conditioning of the  $D_t$  operator [32].

Figure 1, Figure 2, and Figure 3 illustrates the condition number of the matrix  $E^{-1}$  using uniform time sampling with  $2K + 1$  instances for  $K$  values of 2, 3, and 4 respectively. The first two frequencies  $\omega_1$  and  $\omega_2$ , range from 1 rad/s to 750 rad/s with a resolution of 0.5 rad/s, while for the case of  $K = 3$  and  $K = 4$ , only specific frequencies for  $\omega_3$  and  $\omega_4$  have been chosen.

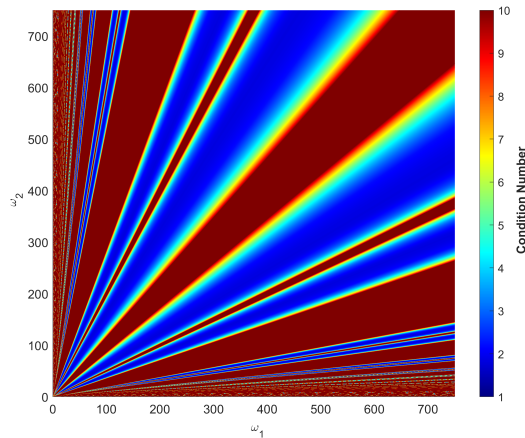


Figure 1: Condition number of matrix  $E^{-1}$  for  $K = 2$ .

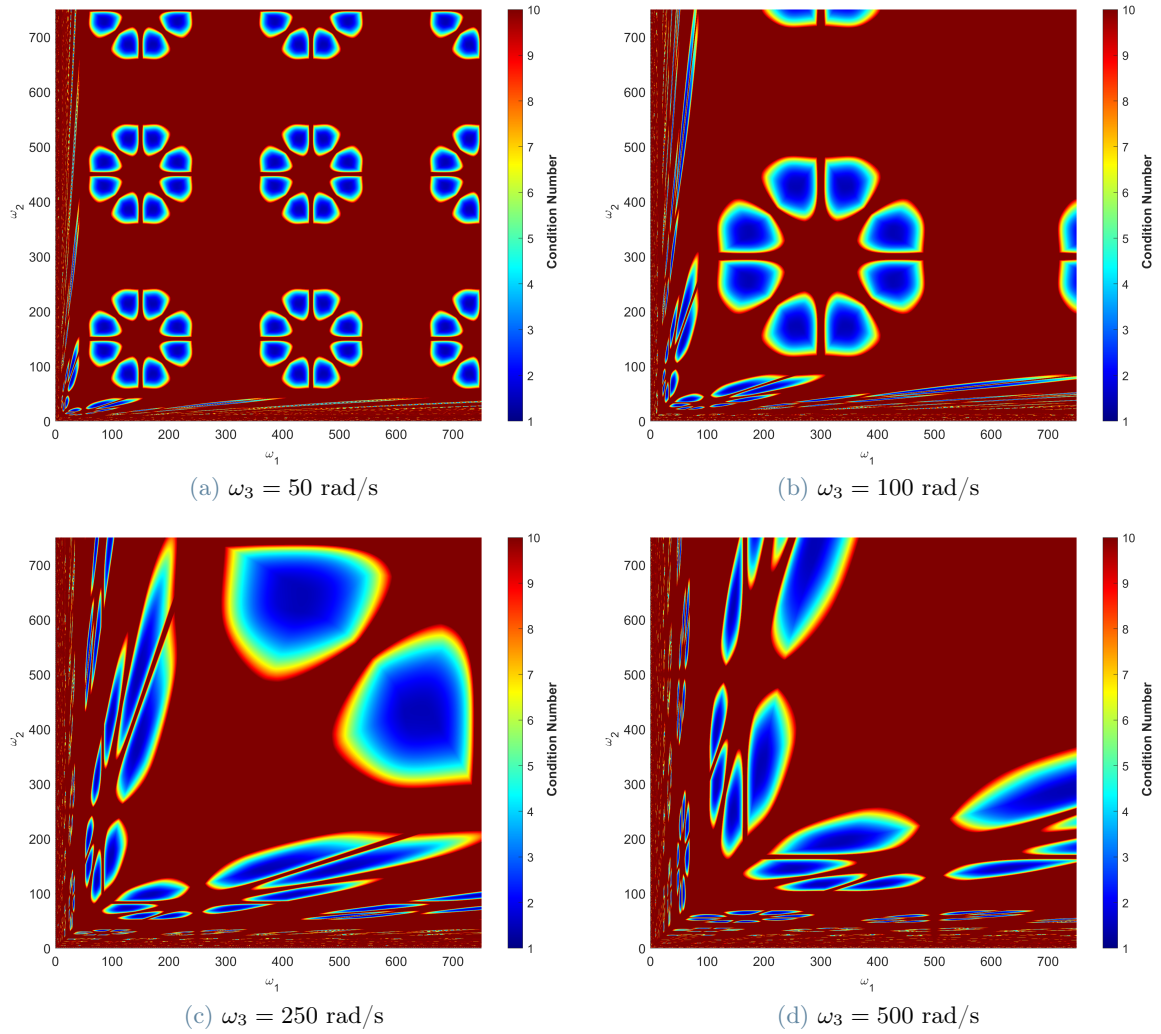


Figure 2: Condition number of matrix  $E^{-1}$  for  $K = 3$ .

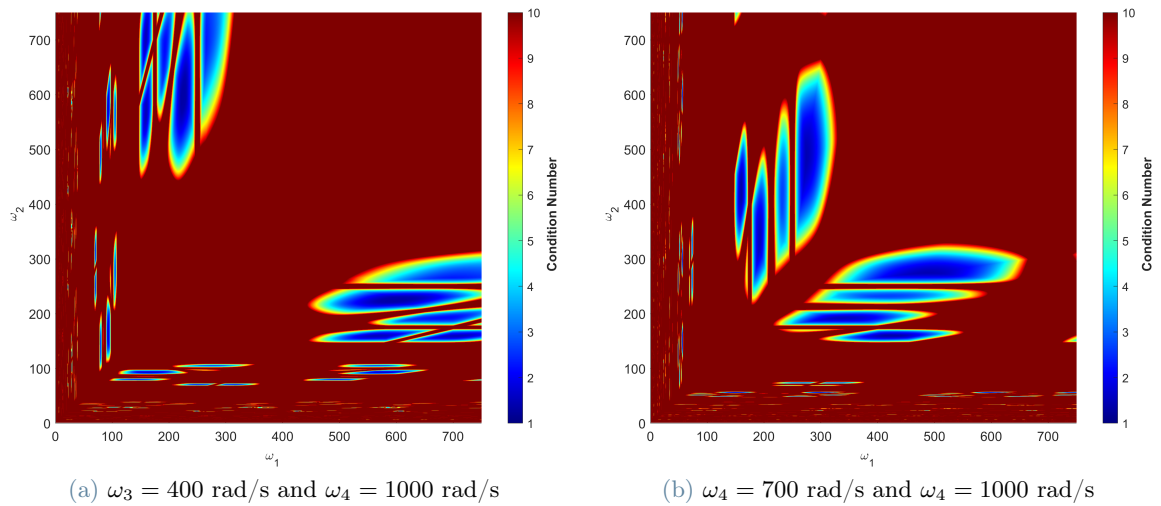


Figure 3: Condition number of matrix  $E^{-1}$  for  $K = 4$ .

From these figures, it can be seen that as  $K$  increases which corresponds in increasing number of the input frequencies for the Harmonic Balance method, the uniform time sampling approach becomes more and more unstable. Also, choosing frequencies close to each other, which corresponds to the region near the bisector of the first quadrant, or choosing frequencies very far from each other, which corresponds to the region near the x

or y axis (the plot is symmetric with respect to bisector), can lead to high condition number. Furthermore, as  $K$  increases, the region near the origin (which corresponds to frequencies with lower values) becomes unstable and the sensitivity of these input frequencies on condition number also increases.

### 3.2. OptTP algorithm

To solve these stability issues, extensive work has been done in recent years, and many solutions have been proposed [14, 31, 32]. In this work, OptTP algorithm [14] has been proposed and the starting point of this algorithm is based on the fact that the IDFT matrix depends on two parameters, the input frequencies ( $\omega_k$ ) and the time instances ( $t_n$ ). Since the input frequencies are already chosen by the user, the only remaining parameter to stabilize the IDFT matrix are the time instances. Given the adoption of uniform time sampling, these time instances are determined solely by the time period  $T_0$ , which corresponds to the time period obtained from the smallest input frequency  $\omega_{min}$  as  $T_0 = 2\pi/\omega_{min}$ .

Consequently, this method consists in finding an optimal time period  $T^*$  which varies from an interval of time periods  $T_0$  to  $T_{max}$  with a certain step size of  $\Delta T$  for which the condition number of the IDFT matrix is minimized. Both the maximum time period,  $T_{max}$  and the step size  $\Delta T$  are defined by the user. In Figure 4, the condition number of IDFT matrix is drawn in the case of  $K = 2$  with  $\omega_1 = 100$  rad/s and  $\omega_2 = 270$  rad/s with the time period  $T$  ranging from  $T_0 = 2\pi/\omega_1$  to  $T_{max}=5T_0$  with  $\Delta T = 0.01T_0$ . The figure clearly illustrates that the condition number changes with  $T$  and displays several local minima. By selecting the time period of  $T^*=1.7294T_0$ , which corresponds to the global minima, the condition number decreases from 4.0258 to 1.71286. Consequently, the optimal time period,  $T^*$  is selected and the new vector of time instances  $t^*$ , is uniformly sampled with  $2K + 1$  instances with  $t_n^* = (n - 1)T^*/N$ .

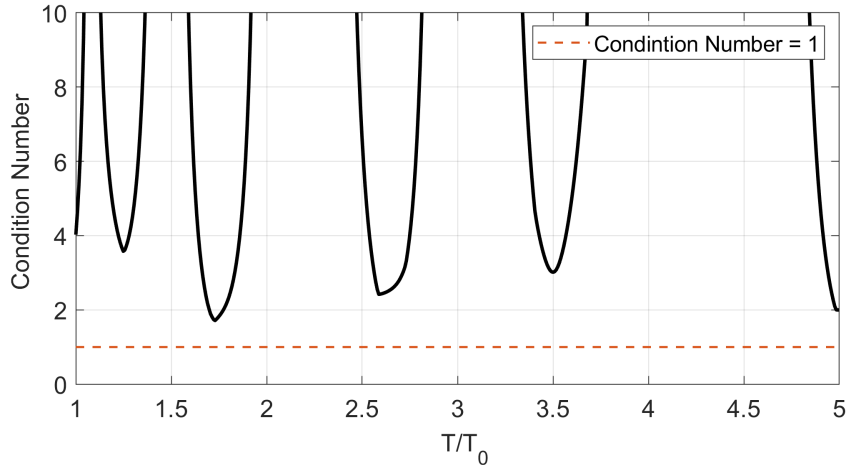


Figure 4: Variation of the Condition number with respect to time period  $T$ .

In Figure 5, the condition number of IDFT matrix for  $K$  values of 2, 3, and 4 after applying the OptTP method has been plotted. The first two frequencies  $\omega_1$  and  $\omega_2$ , range from 1 rad/s to 750 rad/s with a resolution of 0.5 rad/s, while for the case of  $K = 3$  and  $K = 4$ , only specific frequencies for  $\omega_3$  and  $\omega_4$  have been chosen. The reduction in the condition number is evident across the majority of input frequencies. However, as the number of input frequencies ( $K$ ) increases, the efficiency of this method tends to diminish. An important remark must be made about decreasing the condition number of the IDFT matrix. Decreasing the condition number has an impact on only reducing the amplification of input errors, however, this reduction doesn't necessarily lead to an acceleration in the convergence of the solution. The speed at which the solution converges depends upon various factors, such as mesh quality, the numerical techniques employed for solving linear systems, the effectiveness of pre-conditioning methods.

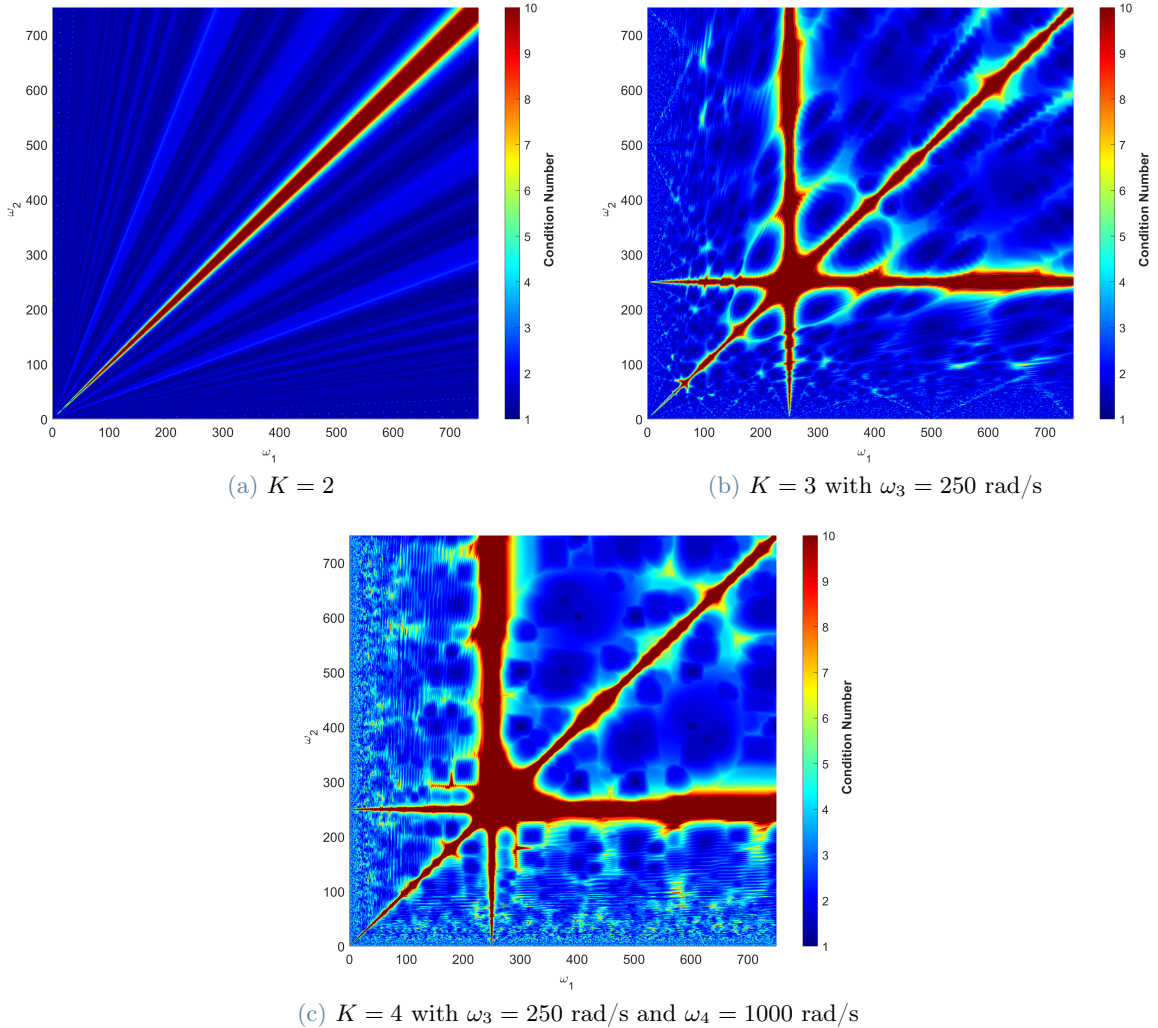


Figure 5: Condition number of matrix  $E^{-1}$  after applying OptTP algorithm.

In SU2, this algorithm is applied at the beginning of the simulation to determine the time period for which the IDFT matrix has the minimum condition number. Typically, as the optimal time period  $T^*$  increases, the error in the solution also increases. This is due to a reduced sampling rate resulting from a longer time period, leading to aliasing errors and additional corruption of the interpolated solution. Furthermore, the Harmonic Balance method attempts to fit the solution based on an incorrect basis over a larger time interval, compromising the accurate representation of local variations in the solution. So, instead of choosing the global minima of the condition number, usually,  $T^*$  is chosen to be the first time period,  $T$ , for which the local minima of the condition number is smaller than the condition number of the initial time period  $T_0$ [14].

## 4. Results

In this section, the test cases and the verification results are presented. The first test case compares the accuracy of the solution obtained from Harmonic Balance method with a time-accurate solution using a 2D geometry. Next, a simple 3D geometry is employed to perform the same evaluations and then the solutions obtained from these simulations were utilized for comparing the aeroacoustic noise propagation results using the Farassat's 1A formulation. Finally, a more practical test case of a propeller was used to further assess and compare the aeroacoustic noise propagation results.

### 4.1. 2D NACA64A10 pitching airfoil

For benchmarking the Harmonic Balance method, a 2D NACA64A010 airfoil pitching about its quarter-chord point in viscid flow is used, which is proposed by the SU2 community. A rigid sinusoidal motion around the quarter-chord of the airfoil is imposed by defining a time-varying function of the angle of attack as follows,

$$\alpha(t) = 1.01 \sin(\omega_1 t) \quad (23)$$

where the pitching frequency,  $\omega_1 = 109.339$  rad/s. The simulations were performed using standard conditions for free stream pressure and temperature with a freestream Mach number of 0.4 with a resulting Reynolds number of  $9.319 \times 10^6$ . The convective fluxes were computed using the Jameson-Schmidt-Turkel (JST) scheme, while the turbulent viscosity was calculated using the SA one equation turbulence model. An O-grid structured mesh, available on the SU2 repository, was used which is composed of 12288 elements with 192 elements along the airfoil and 192 elements on the far-field boundary. In figure 6a, the mesh near the airfoil is shown. Concerning the time-accurate simulation, a  $2^{nd}$  order dual time stepping method was used to solve URANS equations. The simulation was performed for  $10T$ s where  $T = 2\pi/\omega_1$ , is the period corresponding to the pitching frequency. A total of 600 physical time steps were simulated and for each physical time step, 40 inner iterations were performed. Regarding harmonic balance, three simulations were performed using three set of frequencies as shown in table 1 using a total of 40000 iterations.

No. of Frequencies	Set of Frequency
K=1	$\underline{\omega} = [0, \omega_1, -\omega_1]^T$
K=2	$\underline{\omega} = [0, \omega_1, 2\omega_1, -\omega_1, -2\omega_1]^T$
K=3	$\underline{\omega} = [0, \omega_1, 2\omega_1, 3\omega_1, -\omega_1, -2\omega_1, -3\omega_1]^T$

Table 1: Set of frequencies used for Harmonic Balance simulation.

In figure 6b, the Mach field around the airfoil obtained from the time-accurate simulation at maximum angle of attack is shown. No shocks are present in the flow field, no big flow separation occurs even when the maximum angle of attack is reached since the amplitude of the oscillation is very low.

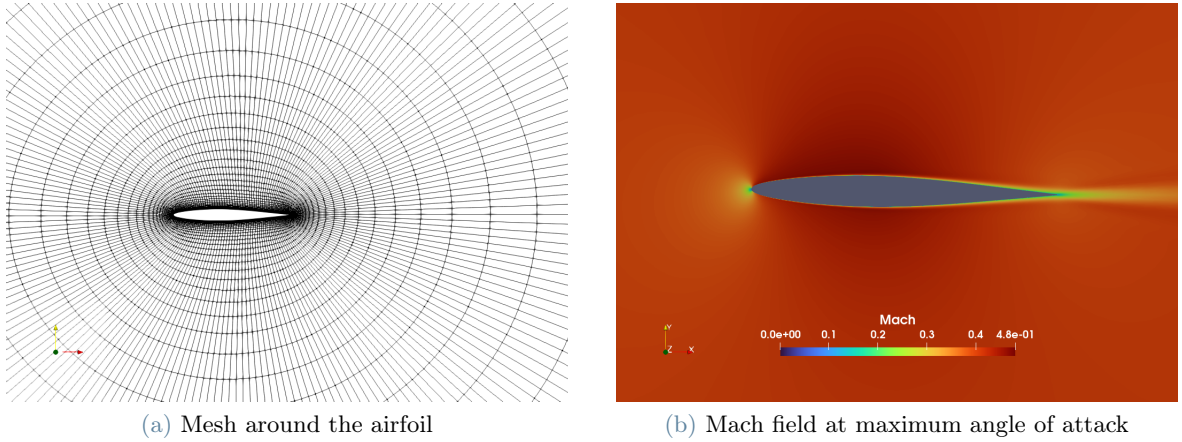


Figure 6: 2D NACA 64A10 airfoil

In figure 7a and figure 7b, a comparison of lift and drag coefficient is made between the time-accurate simulation (URANS) and Harmonic balance simulation (HB), each with and without spectral interpolation. There is an excellent agreement between the time-accurate simulation and Harmonic Balance even when a single frequency is used. In table 2, the maximum lift coefficient ( $C_{l_{max}}$ ) and maximum drag coefficient ( $C_{d_{max}}$ ) obtained from time-accurate simulation and Harmonic Balance simulations are compared with their corresponding relative error ( $Error_{rel}\%$ ). As the number of input frequencies  $K$  increases, the accuracy of Harmonic Balance increases and in this case, even one input frequency is sufficient to represent accurately the lift and drag coefficients. Any small deviations from the time-accurate solution can be attributed to the presence of other harmonic content in the flow due to non-linear phenomena generated in the boundary layer.

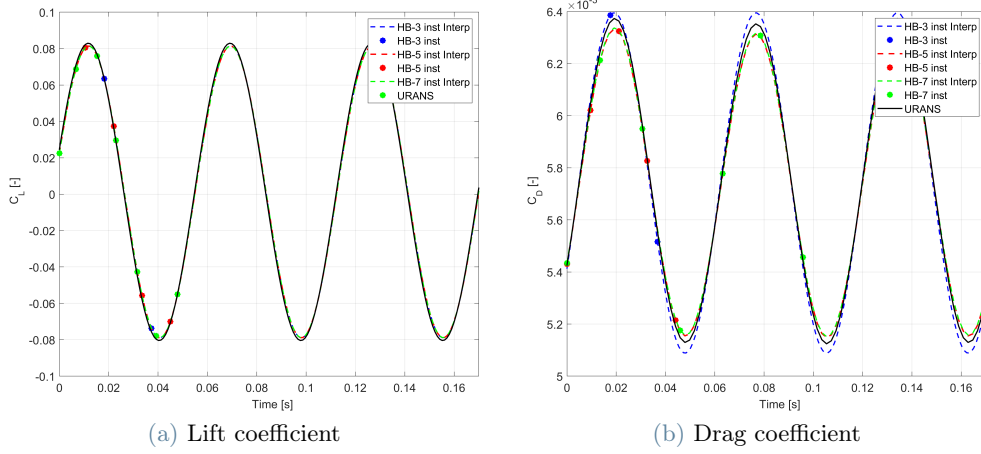


Figure 7: Comparison of Harmonic Balance solution with time-accurate solution.

	$C_{l_{max}}$	$ Error_{rel}\% $	$C_{d_{max}}$	$ Error_{rel}\% $
URANS	0.082916	-	0.00635268	-
HB-3 inst	0.0813366	1.90542959	0.00639397	0.649961906
HB-5 inst	0.0814281	1.79446689	0.00631303	0.62414603
HB-7 inst	0.0814841	1.726928458	0.0063132	0.62146994

Table 2: Comparison of maximum lift and drag coefficient

To further investigate the discrepancies in the solution, in figure 8, the pressure at several locations on the airfoil is plotted from all the simulations. The locations where the pressure is measured are shown in figure 8. A good agreement is reached for most of the locations on the airfoil, except in the region near the leading and trailing edge.

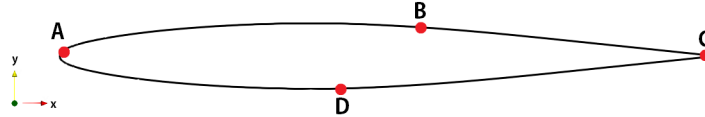
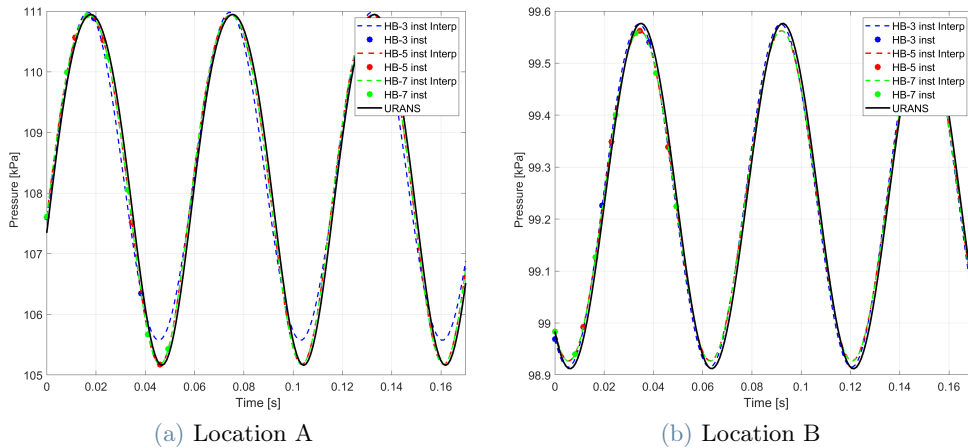


Figure 8: Locations where the pressure is measured.



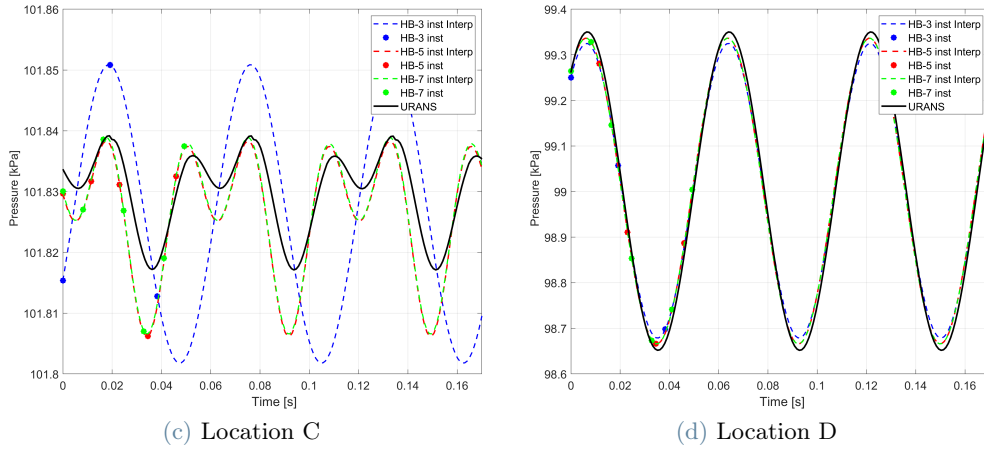


Figure 8: Comparison of pressure obtained from Harmonic Balance and Time-accurate solution.

Applying the Fourier transform to these pressure variations (only the magnitude of the Fourier coefficients is represented) obtained from the time-accurate solution (figure 9), it is clear that in the wake region, additional harmonics are present which degrade the quality of the solution obtained from Harmonic Balance method as these harmonics were not simulated. The frequency spectrum also shows the dominant frequencies in the flow field which are also the input frequencies chosen for the Harmonic Balance simulation, thus giving excellent results. It is also important to highlight that increasing the number of frequencies doesn't always result in a significant increase in accuracy as demonstrated by simulating a third frequency ( $3\omega_1$ ). In figure 9, it is evident that the third frequency doesn't contribute much to the harmonic content of the pressure time history, thus resulting in a very limited increase in the accuracy of the solution.

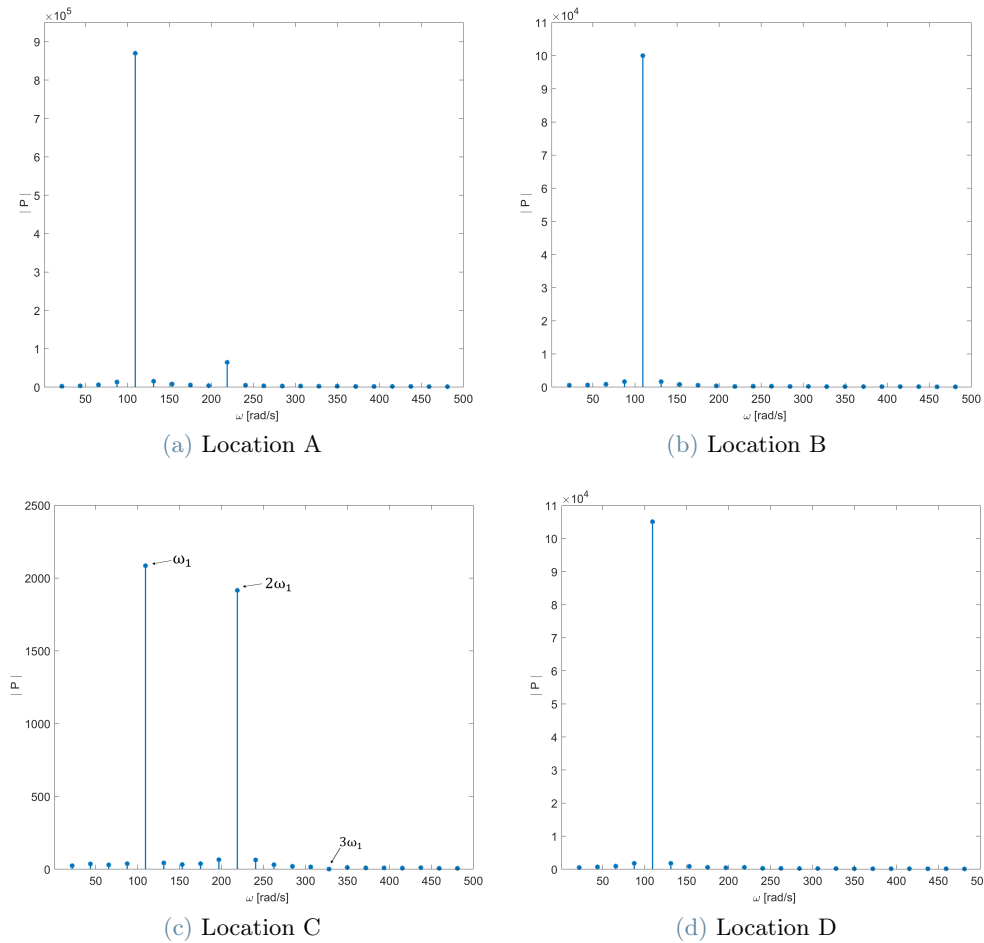


Figure 9: Frequency spectrum of the pressure measured in the same locations.

## 4.2. 3D NACA6410 rectangular wing

To evaluate the aeroacoustic noise propagation using the flow solution from Harmonic Balance method, a 3D NACA6410 rectangular pitching wing immersed in a uniform flow is used. The wing has a chord of  $1m$  and a wingspan of  $3m$  (figure 10a). The computational mesh is made using Pointwise and it consists of a cylinder of radius  $50m$  and height  $40m$  (figure 10a). The wing is placed in the middle of the cylinder with the origin of the reference frame in the quarter-chord point in the mid-span of the wing. To reach a  $y^+$  value of 1, boundary layer cells were added with the height of the first cell being  $2\mu m$ , and for the rest of the computational domain, unstructured mesh was used (figure 10c). The free-stream conditions, the change of angle of attack in time, and all the simulation parameters are chosen to be the same as the 2D NACA6410A pitching airfoil test case. Even in this case, two sets of input frequencies were used for the Harmonic Balance method. The first one being  $[0, \omega_1, -\omega_1]$  and the second being  $[0, \omega_1, -\omega_1, \omega_2, -\omega_2]$  where  $\omega_1=109.339$  rad/s and  $\omega_2=2*\omega_1$ . For the time-accurate solution again a  $2^{nd}$  order dual time stepping method was used to solve the URANS equations.

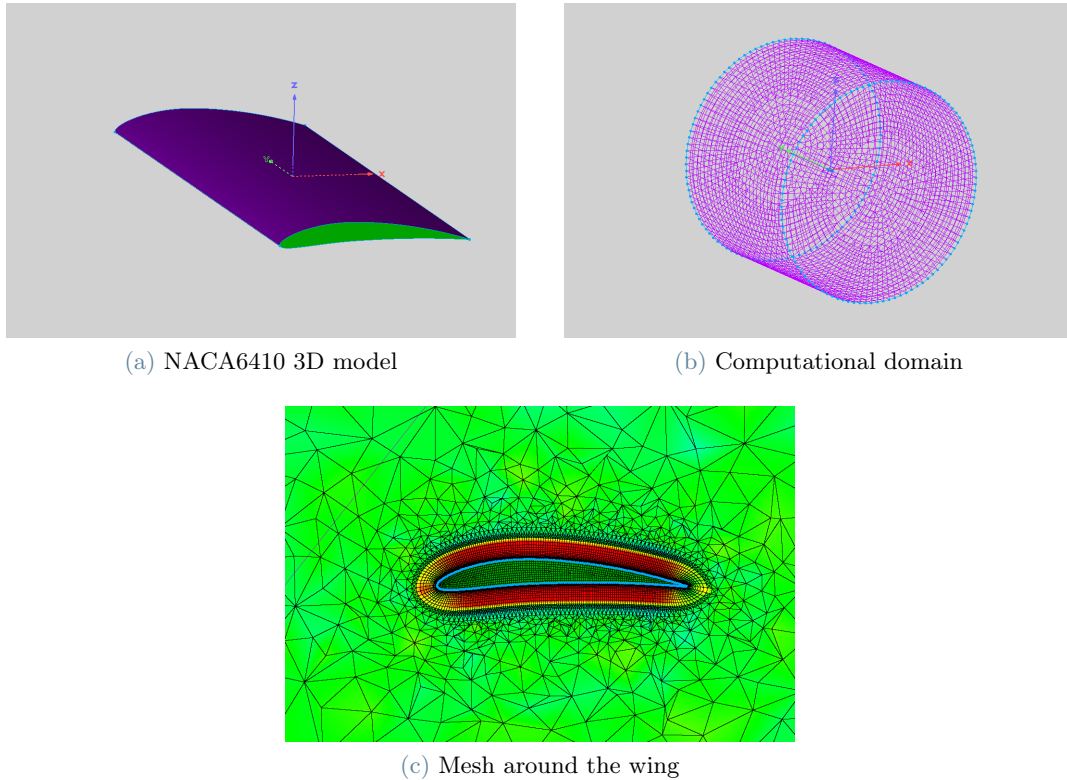


Figure 10: Geometry and domain

In the figure 11a and figure 19b, the pressure distribution over the suction side and pressure side of the wing is shown. The flow is smooth over the whole wing except near the wingtips, where on the suction side, wingtip vortices are present.

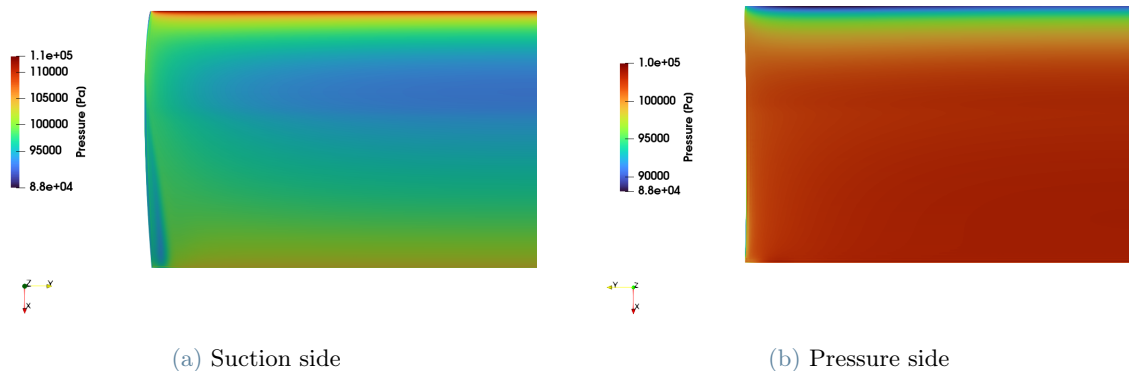


Figure 11: Pressure distribution over half wing

In figure 12a and figure 12b, a comparison of lift and drag coefficient is made between the solution obtained from time-accurate simulation (URANS) and Harmonic Balance method (HB) using the two sets of input frequencies mentioned before. In this case, a single frequency is not sufficient to predict accurately the drag coefficient but by increasing the number of input frequencies, the accuracy is improved. This occurs in the 3D case because the flow field is more intricate due to the presence of wingtip vortices which interact with the wake region behind the wing greatly affecting the drag coefficient.

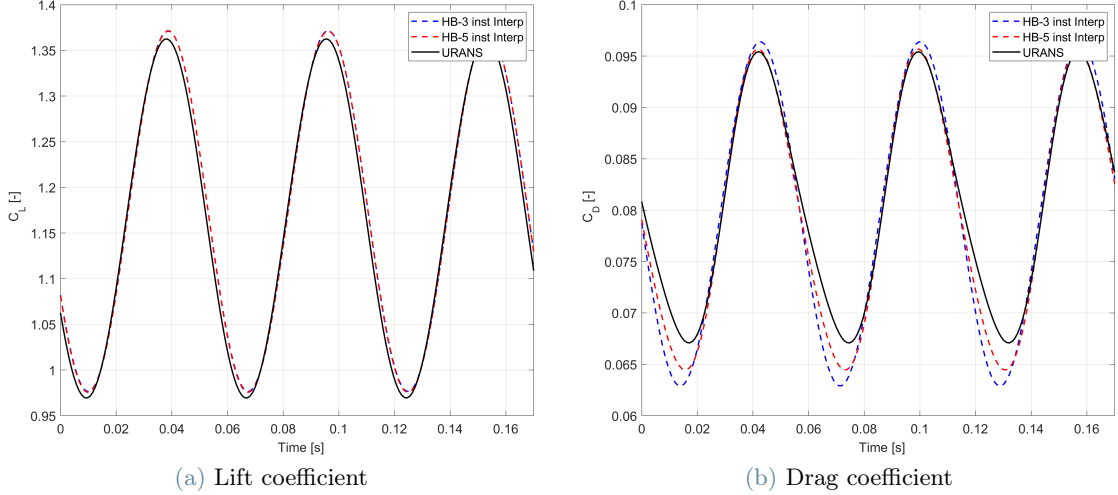


Figure 12: Comparison of Harmonic Balance solution with time-accurate solution.

Once the surface flow solution is available from the Harmonic Balance method and the time-accurate method, the aeroacoustic noise propagation is performed using the CAA module provided with SU2. In figure 21, the distribution of observer locations (mics), where the noise is propagated, around the wing is shown. 120 uniformly distributed observers are placed along a circumference of radius  $R$  centered in the mid-span of the wing. The coordinate  $\Phi$  denotes the angular position of the observer location on the circumference with  $\Phi = 0^\circ$  being the position of the observer placed directly behind the trailing edge.

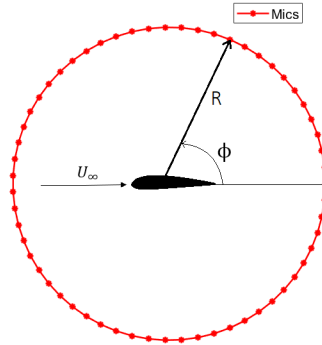
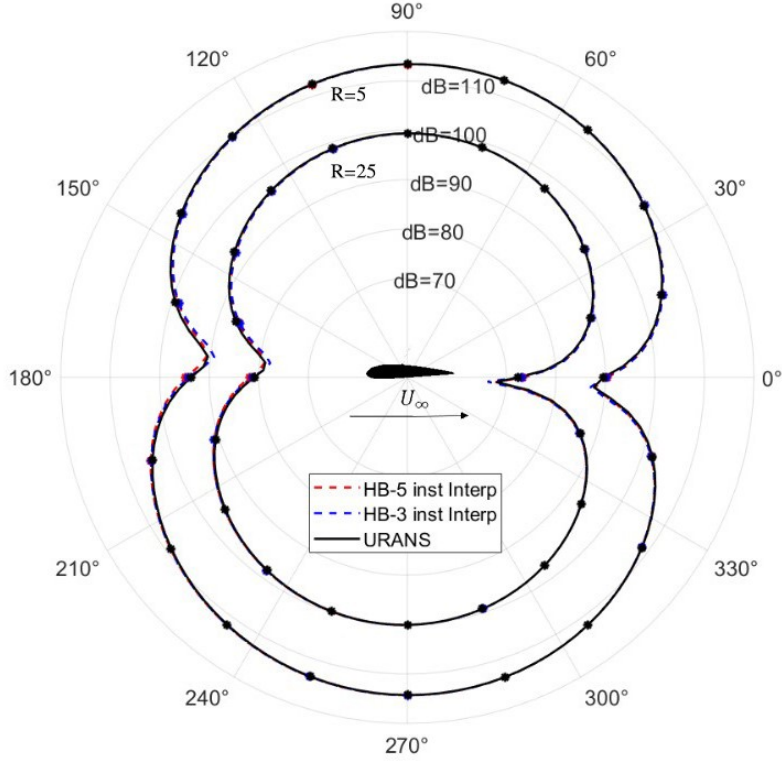


Figure 13: Microphone distribution at mid-span around the wing

In figure 14, the directivity plot for the radius  $R = 5m$  and  $R = 25m$  is shown. At every location (for clarity, every 6th value of SPL is highlighted), the Sound Pressure Level (SPL) was computed as

$$SPL = 20 \log \left( \frac{p_{rms}}{p_{ref}} \right) \quad (24)$$

Where  $p_{rms}$  is the root mean square value of the pressure fluctuation and  $p_0$  is the reference value of  $2 * 10^{-6} Pa$ .



+

Figure 14: Directivity plot around the mid-span of the wing at different distances

Overall the agreement is excellent in all directions even when a single frequency for the Harmonic Balance method is used, except for the region near the trailing edge (downstream) and leading edge (upstream). In table 4 and table 3, SPL values and their relative error ( $Error_{rel}\%$ ) compared to the time-accurate solution are reported for certain angular positions ( $\Phi$ ), at the radius of  $R = 5m$  and  $R = 25m$  respectively.

$\Phi$	$-30^\circ$	$-15^\circ$	$-3^\circ$	$0^\circ$	$3^\circ$	$15^\circ$	$30^\circ$	$60^\circ$	$165^\circ$
URANS	91.72	86.72	74.70	78.36	72.31	85.90	91.95	97.56	86.40
HB-3 inst	91.64	86.51	73.49	77.14	73.07	86.21	92.12	97.62	85.59
$ Error_{rel}\%$	0.085	0.237	1.617	1.555	1.043	0.356	0.185	0.063	0.930
HB-5 inst	91.65	86.56	73.97	78.34	73.29	86.18	92.10	97.61	85.81
$ Error_{rel}\%$	0.069	0.184	0.966	0.029	1.348	0.321	0.160	0.051	0.683

Table 3: Comparison of SPL in dB with its relative error at  $R = 25m$

$\Phi$	$-30^\circ$	$-15^\circ$	$-3^\circ$	$0^\circ$	$3^\circ$	$15^\circ$	$30^\circ$	$60^\circ$	$165^\circ$
URANS	105.91	100.25	87.69	89.61	93.68	102.67	107.75	112.43	97.32
HB-3 inst	105.77	99.91	87.01	90.17	94.28	102.96	107.91	112.48	96.31
$ Error_{rel}\%$	0.130	0.342	0.777	0.629	0.642	0.277	0.147	0.044	1.035
HB-5 inst	105.82	100.03	87.83	90.40	94.030	102.91	107.88	112.46	96.60
$ Error_{rel}\%$	0.088	0.223	0.159	0.888	0.655	0.234	0.116	0.026	0.746

Table 4: Comparison of SPL in dB with its relative error at  $R = 5m$

Overall, the relative error remains less than 0.5% for the region above and below the wing even when a single

frequency is used and by increasing the number of input frequencies, the error tends to decrease. In figure 14 and tables 3 and 4 it can also be observed that as the distance of the observer location increases with respect to the wing, the relative error between the sound pressure level (SPL) evaluated in the region above and below the wing, also decreases. As the distance increases, the terms present in the Farassat's 1A formulation that are proportional to  $(1/R^2)$  which are dominant in the near-field die out quickly relative to terms proportional to  $(1/R)$  that are dominant in the far-field which further enhances the precision of the noise propagation by employing the Farassat 1A formulation.

In figure 17 and figure 16, a comparison between the time history of pressure fluctuations obtained from CAA module using the Harmonic Balance solution and time-accurate simulation is made. The observers in figure 17 are positioned directly behind the trailing edge ( $\Phi = 0^\circ$ ) at two different distances ( $R = 5m$  and  $R = 25m$ ), while the observers in figure 16 are positioned directly above the suction side of the wing ( $\Phi = 90^\circ$ ) at the same distances.

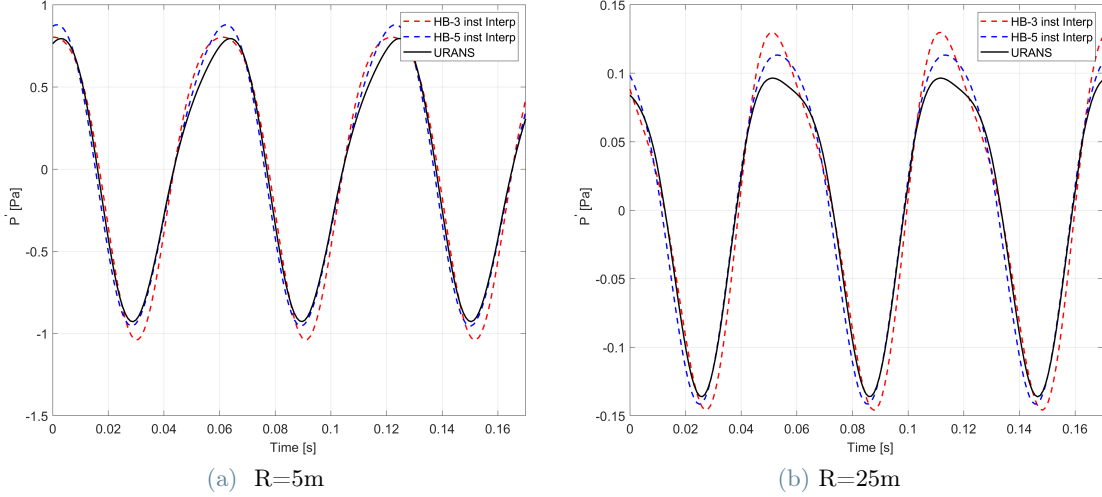


Figure 15: Pressure fluctuations measured at  $\Phi = 0^\circ$ .

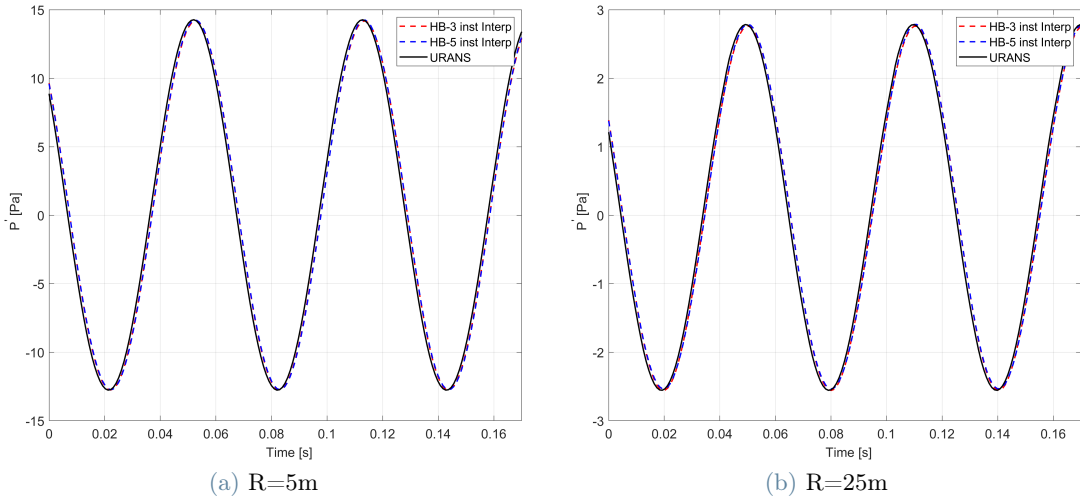
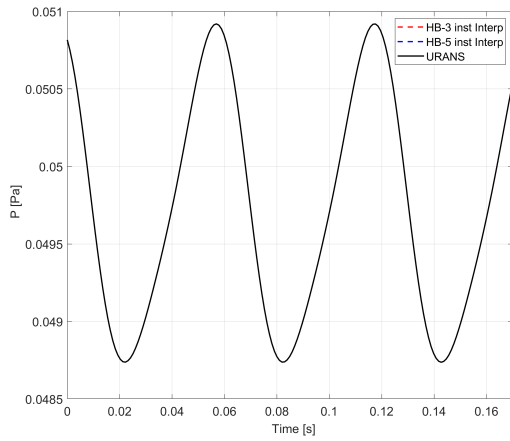
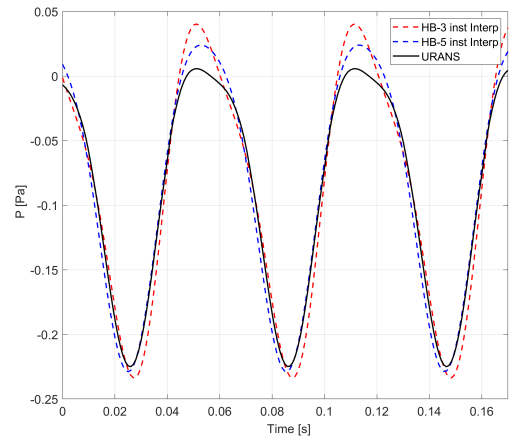


Figure 16: Pressure fluctuations measured at  $\Phi = 90^\circ$ .

As expected, a good agreement is found in the case of  $\Phi = 90^\circ$ , while in the case of  $\Phi = 0^\circ$ , more harmonics are required to better capture the pressure fluctuations. This behavior was also observed in the directivity plot (figure 14), where the maximum relative error was found in the region in front of the leading edge and behind the trailing edge. Breaking down these pressure fluctuations into the loading noise and thickness noise components, as illustrated in figure 17 and figure 16, reveals that the primary source of error originates from the loading noise component. Examining the pressure coefficient ( $C_P$ ) distribution over some sections of the wing (figure 18), it is apparent that in these regions there is a drastic variation of pressure on the wing surface which introduces non-linearities and consequently additional harmonics[33].

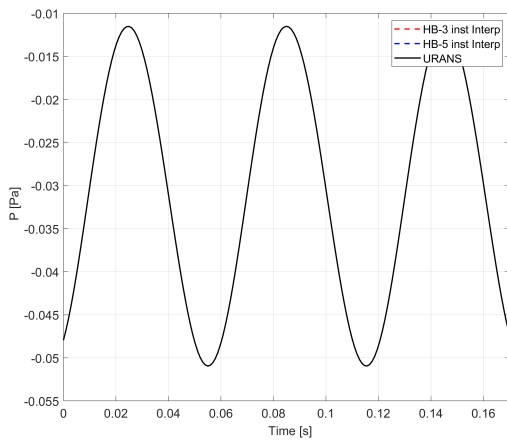


(a) Thickness noise

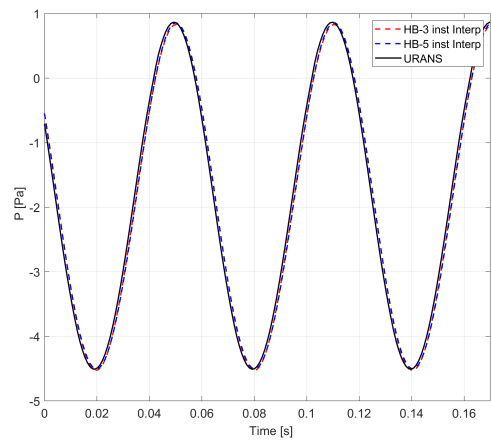


(b) Loading noise

Figure 17: Pressure components measured at  $\Phi = 0^\circ$  and  $R=25m$ .

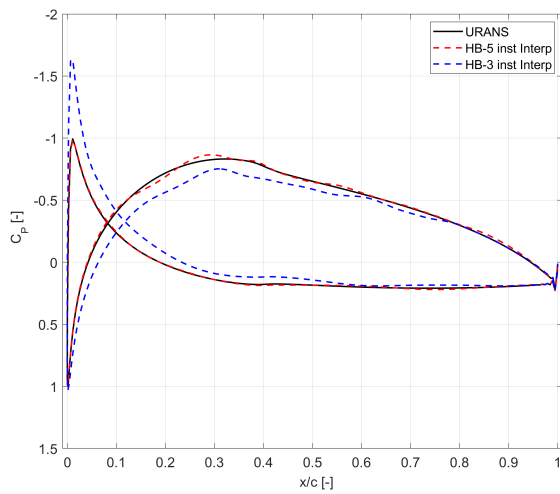


(a) Thickness noise

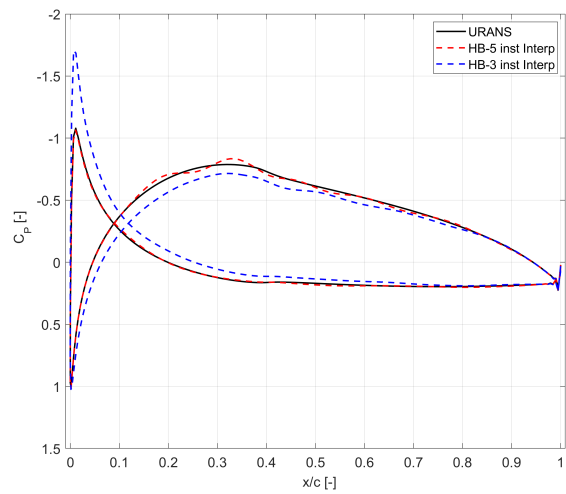


(b) Loading noise

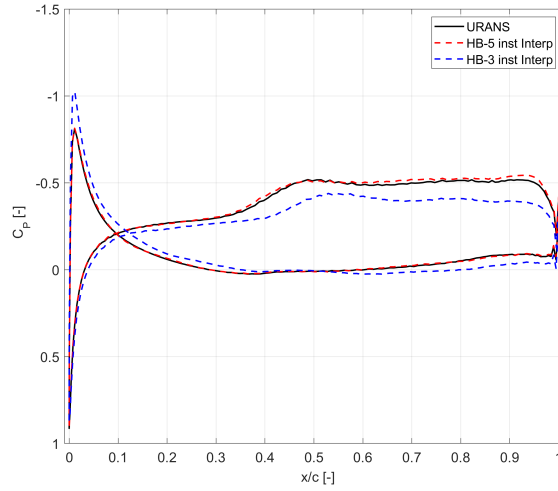
Figure 18: Pressure components measured at  $\Phi = 90^\circ$  and  $R=25m$ .



(a) 50% of wingspan



(b) 25% of wingspan



(c) 1% of wingspan

Figure 18: Pressure coefficient distribution over different sections of the wing at maximum angle of attack.

### 4.3. Isolated propeller in uniform flow

To further evaluate the aeroacoustic noise propagation using Harmonic balance, a real-world test case of a rigid isolated propeller of an eVTOL aircraft in uniform flow, is studied. The propeller that is used is a three-blade hub consisting of left-handed VarioProp 12C blades with a disk diameter  $D$  of  $300\text{mm}$  and a  $65\text{mm}$  diameter spinner installed on the propeller hub (figure 19). The propeller's 3D geometric CAD model was obtained through a 3D scanning of the blades[34, 35].

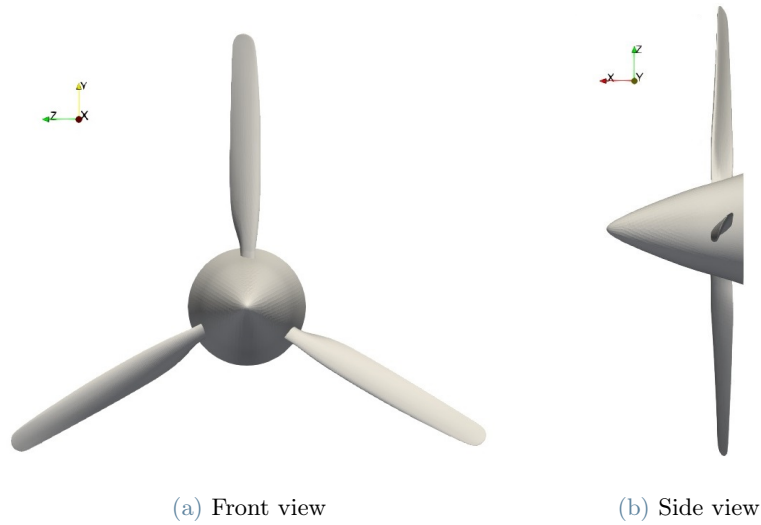


Figure 19: 3D model of the propeller

The computational mesh was obtained using Pointwise. The maximum  $y^+$  value obtained at the first cell in the normal direction is 1.8 with a total number of cells equal to  $18.0 \times 10^6$ . In figure 20, the discretized blade surface is shown.

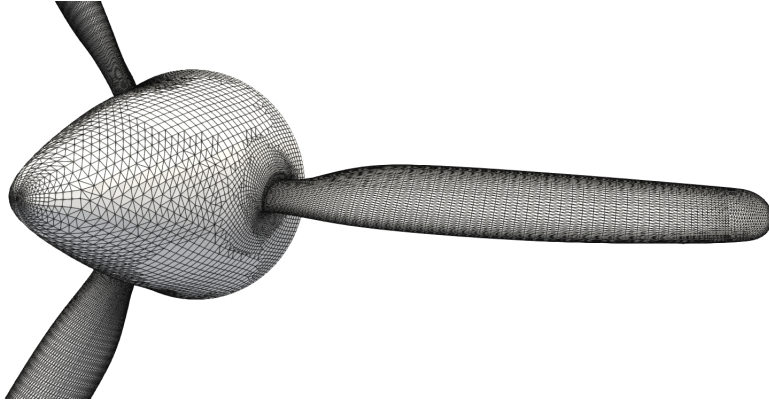


Figure 20: Surface discretization of the propeller

The simulations are performed at a reference temperature of  $294.5K$  and reference density of  $1.18kg/m^3$  with the pitch angle of the rotor set to  $23.3^\circ$ . The rotational speed of the propeller is set to  $7050RPM$  which results in a typical tip Mach number of  $M_t = 0.325$  which also corresponds to the  $M_t$  of the full-scale eVTOL aircraft's propeller in cruise flight condition. The free-stream velocity,  $U_\infty$  is parallel to the axis of rotation of the propeller to simulate the wind tunnel configuration and is chosen by setting the advance ratio  $J$  to 0.8 which is representative of typical cruise flight conditions and is defined as,

$$J = \frac{U_\infty}{nD} \quad (25)$$

Where  $n$  is rotor speed in  $rev/s$ .

The time-accurate simulation was carried out by solving the URANS equations using the dual time-stepping method. Convergence was achieved by simulating six rotations of the propeller, with each physical time step corresponding to one degree of rotation. Spalart-Allmaras turbulence model[36] is used with the algebraic BCM transition model[37] considering a freestream turbulence intensity of 0.1% while the Convective fluxes are solved using JST numerical scheme with 0.5 and 0.005 as 2nd and 4th order dissipation coefficients, respectively. The gradients of the variables at each node are reconstructed using the Green-Gauss theorem. The harmonic balance simulation was performed using a single input frequency ( $K = 1$ ) with  $\underline{\omega} = [0, \omega_1, -\omega_1]^T$ , where  $\omega_1 = 738.2743rad/s$ , using a total of 35000 iterations.

The solutions obtained using harmonic balance simulation and time-accurate simulation are used to compute the aeroacoustic noise emitted by the propeller using CAA module in SU2. The aeroacoustic noise is propagated to 19 locations equally distributed from  $\varphi = 10^\circ$  to  $\varphi = 170^\circ$  at fifteen times the blade radius in the axisymmetric plane of the propeller as shown in figure 21.

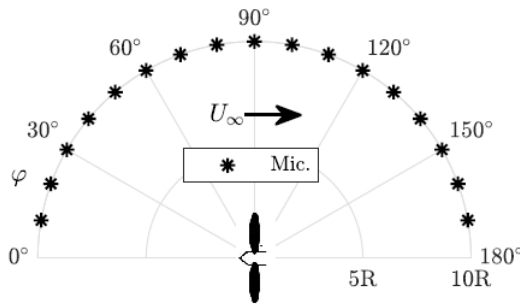


Figure 21: Microphones distribution

At these locations, the Sound Pressure Level (SPL) in dB is calculated with its relative error and shown in figure 22a and figure 22b, respectively. The relative error between the SPL computed by harmonic balance and the time-accurate simulation is less than 0.4% for almost all of the angular positions ( $\varphi$ ) and tends to increase as  $\varphi$  approaches the axis of rotation of the propeller.

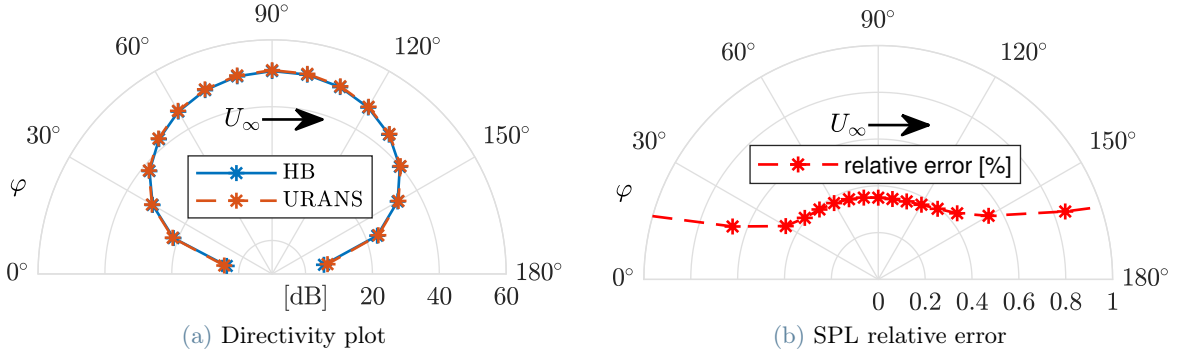


Figure 22: SPL comparison between Harmonic balance and time-accurate simulation

In figure 23, the directivity spectrum of the absolute error between the Harmonic Balance simulation and the time-accurate simulation is shown. Overall, the absolute error is in the order of magnitude of  $10^{-5}$  and tends to increase in the presence of higher harmonics which were not included in the simulation.

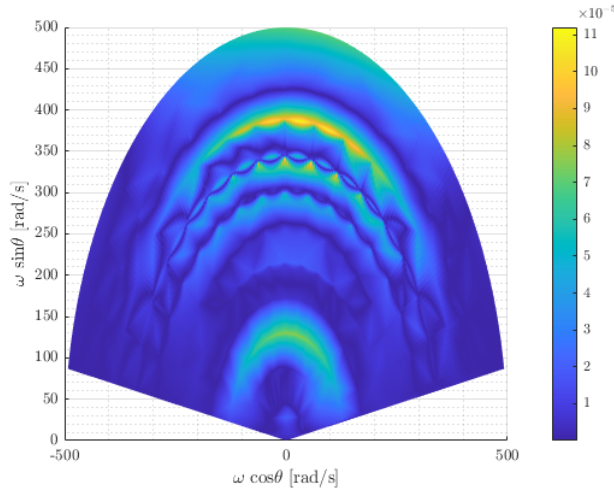


Figure 23: Directivity spectrum of absolute error

## 5. Conclusions

In this paper, the effectiveness of the Harmonic Balance (HB) method for solving quasi-periodic unsteady flows was studied. This method has demonstrated significant advantage in terms of computational efficiency compared to traditional time-accurate approaches, making it a cost-effective technique for accurately computing unsteady flows. Spectral interpolation was implemented to increase the limited time resolution of the solution obtained from the Harmonic Balance method. To overcome the stability issues related to the choice of input frequencies, a simple and robust, OptTP algorithm was implemented. The results were compared with the time-accurate solution and even when a single frequency was used, this method was able to capture the dominant aspects of the flow field, especially in the case of integral quantities like the lift coefficient and drag coefficient and by increasing the number of input frequencies, the accuracy of the model can be increased. Furthermore, this method was coupled with the CAA module based on Ffowcs Williams and Hawkings equation present in SU2 to investigate aeroacoustic noise propagation. Only the surface flow solution was used to propagate the pressure disturbances and the tonal noise at different locations was analysed. Even in this case, the Harmonic Balance method has demonstrated its potential and by using a single frequency, the relative error of sound pressure level (SPL) obtained using the Harmonic Balance method and the time-accurate method was less than 2%. The main source of the error was identified to be the loading noise component which depends on the pressure variations on the surface of the body. Consequently, this lead to a greater error in the vicinity of both the leading and trailing edges. However, by increasing the number of harmonics, the relative error tends to decrease. In summary, the results of this work clearly illustrate the advantages of using this reduced-order model for performing quasi-periodic unsteady simulations and aeroacoustic noise prediction. In future work, instead of using simplified test cases, a real-world case of a whole helicopter or drone could be simulated using the Harmonic Balance method

and using additional frequencies, other effects like interference, Blade-Vortex Interactions (BVI), or high-speed impulsive noise can be modelled and investigated.

## 6. Acknowledgments

I would like to express my sincere gratitude to Prof. Alberto Guardone and Politecnico di Milano, for granting me this opportunity and the essential resources necessary for the completion of this thesis. I also extend my heartfelt appreciation to my supervisor, Dr. Luca Abergo for his invaluable guidance, unwavering support, and constructive feedback throughout the entire process of researching and writing this thesis, including the tasks of providing and meshing the geometries.

## References

- [1] N. Gourdain, L. Gicquel, R. Fransen, E. Collado, and T. Arts. "application of rans and les to the prediction of flows in high pressure turbine components". *ASME Turbo Expo, GT2011-46518*,, page 1773–1785, 2011. <https://doi.org/10.1115/GT2011-46518>.
- [2] P. Sagaut and S. Deck. "large-eddy simulation for aerodynamics: status and perspectives". *Philosophical Transactions of the Royal Society A* 367, page 2849–2860, 2009. <http://www.jstor.org/stable/40485630>.
- [3] A. Jameson, J. Alonso, and M. McMullen. "application of a non-linear frequency domain solver to the euler and navier-stokes equations". *40th AIAA Aerospace Sciences Meeting and Exhibit, Vol. 236*, page 120, 14 January 2002 - 17 January 2002. <https://doi.org/10.2514/6.2002-120>.
- [4] Beckett Yx Zhou, Tim A. Albring, Nicolas R. Gauger, Thomas D. Economon, and Juan J. Alonso. "an efficient unsteady aerodynamic and aeroacoustic design framework using discrete adjoint". *17th AIAA/ISSMO multidisciplinary analysis and optimization conference*, page 3369, 2016. <https://doi.org/10.2514/6.2016-3369>.
- [5] Wendt Kristin and Asmer Lukas. Urban air mobility in europe-assessment of technology development and market potential from research and industry perspective. In *AIAA Aviation 2022 Forum*, page 3652, 2022.
- [6] Israa Alesbe, Moustafa Abdel-Maksoud, and Sattar Aljabair. "investigation of the unsteady flow behaviour on a wind turbine using a bem and a ranse method, volume 2016". *Journal of Renewable Energy*, pages 1–12, 2016. <https://doi.org/10.1155/2016/6059741>.
- [7] Tandon Vishal, Reddy S. N. Dileep Bushanand, Bharathan R. D, and Ramana Murthy S. V. "unsteady flow analysis of a highly loaded high-pressure turbine of a gas turbine engine". *Proceedings of the National Aerospace Propulsion Conference*, page 119–132, 2020. [https://doi.org/10.1007/978-981-15-5039-3\\_7](https://doi.org/10.1007/978-981-15-5039-3_7).
- [8] A. K. Gopinath, E. van der Weidey, J.J. Alonso, K. Ekici, and K. C. Hall. "three-dimensional unsteady multi-stage turbomachinery simulations using the harmonic balance technique". *45th AIAA Aerospace Sciences Meeting and Exhibit*, page 892, 8 - 11 January 2007. <https://doi.org/10.2514/6.2007-892>.
- [9] L. Hanson, K. Baskaran, S. Pullin, B. Zhou, and M. Azarpeyvand. "aeroacoustic and aerodynamic characteristics of propeller tip geometries". *28th AIAA/CEAS Aeroacoustics Conference*,, June 2022. <https://doi.org/10.2514/6.2022-3075>.
- [10] Straubinger A., Rothfeld R., Shamiyeh M., Büchter K. D. Kaiser J., and Plötner K. O. "an overview of current research and developments in urban air mobility – setting the scene for uam introduction". *Journal of Air Transport Management, Vol. 87*,, page 101852, 2020. <https://doi.org/10.1016/j.jairtraman.2020.101852>.
- [11] Colonius T. and Lele S. K. "computational aeroacoustics: progress on nonlinear problems of sound generation". *Progress in Aerospace sciences, Vol. 40, No. 6*,, page 345–416, 2004. <https://doi.org/10.1016/j.paerosci.2004.09.001>.
- [12] Hall K. C. and Crawley E. F. "calculation of unsteady flows in turbomachinery using the linearized euler equations". *AIAA Journal, Vol. 27, No. 6*,, pages 777–787, 1989. <https://doi.org/10.2514/3.10178>.

- [13] K.C. Hall, J.P. Thomas, and W.S. Clark. "computation of unsteady nonlinear flows in cascades using a harmonic balance technique.". *AIAA Journal*, 40(5), pages 879–86, May 2002. <https://doi.org/10.2514/2.1754>.
- [14] S. Nimmagadda, T.D. Economon, J.J. Alonso, and C.R. Ilário da Silva. "robust uniform time sampling approach for the harmonic balance method". *46th AIAA Fluid Dynamics Conference*, page 3966, 13-17 June 2016. <https://doi.org/10.2514/6.2016-3966>.
- [15] A. Rubino, M. Pini, Colonna P, T. Albring, S. Nimmagadda, T. Economon, and J. Alonso. "adjoint-based fluid dynamic design optimization in quasi-periodic unsteady flow problems using a harmonic balance method". *Journal of Computational Physics, Volume 372*, pages 220–235, 1 November 2018. <https://doi.org/10.1016/j.jcp.2018.06.023>.
- [16] Frédéric Sicot, Guillaume Dufour, and Nicolas Gourdain. "a time-domain harmonic balance method for rotor/stator interactions". *Journal of Turbomachinery, Volume 134, Issue 1*, pages 1–13, January 2012. <https://doi.org/10.1115/1.4003210>.
- [17] Frédéric Sicot, Guillaume Dufour†, and Nicolas Gourdain. "discrete-frequency noise prediction using a harmonic balance method". *ISABE-1131*, 2009. [https://www.cerfacs.fr/~cfdbib/repository/TR\\_CFD\\_09\\_68.pdf](https://www.cerfacs.fr/~cfdbib/repository/TR_CFD_09_68.pdf).
- [18] Guédeney T., Gomar A., Gallard F., Sicot, F. Dufour, and G. Puigt. "non-uniform time sampling for multiple-frequency harmonic balance computations". *Journal of Computational Physics, Vol. 236*, pages 317–345, 2013. <http://dx.doi.org/10.1016/j.jcp.2012.11.010>.
- [19] Gomar A. "multi-frequential harmonic balance approach for the simulation of contra-rotating open rotors : Application to aeroelasticity". *Ph.D. thesis, Ecole nationale supérieure d'arts et métiers-ENSAM*, 2014. <https://hal.science/tel-01077946/>.
- [20] M. Lighthill. "on sound generated aerodynamically. i. general theory.". *Proceedings of the Royal Society*, 211, page 564–587, 1952. <https://doi.org/10.1098/rspa.1952.0060>.
- [21] M. Lighthill. "on sound generated aerodynamically ii. turbulence as a source of sound". *Proceedings of the Royal Society*, 222, page 1–32, 1954. <https://doi.org/10.1098/rspa.1954.0049>.
- [22] F. Farassat and K. S. Brentner. "modeling aerodynamically generated sound of helicopter rotors". *Progress in Aerospace Sciences, Volume 39, Issues 2–3*, pages 83–120, February-April 2003. [https://doi.org/10.1016/S0376-0421\(02\)00068-4](https://doi.org/10.1016/S0376-0421(02)00068-4).
- [23] Hawkings D. L. and Lowson M. V. "theory of open supersonic rotor noise". *Journal of Sound and Vibration, Volume 36, Issue 1*, pages 1–20, 1974. [https://doi.org/10.1016/S0022-460X\(74\)80340-8](https://doi.org/10.1016/S0022-460X(74)80340-8).
- [24] P. Di Francescantonio. "a new boundary integral formulation for the prediction of sound radiation". *Journal of Sound and Vibration, Volume 202, Issue 4*, pages 491–509, 15 May 1997. <https://doi.org/10.1006/jsvi.1996.0843>.
- [25] Thomas D. Economon, Francisco Palacios, Sean R. Copeland, Trent W. Lukaczyk, and Juan J. Alonso. "su2: An open-source suite for multiphysics simulation and design". *AIAA Journal, Vol. 54, No. 3*, pages 828–846, 2015. <https://doi.org/10.2514/1.J053813>.
- [26] Palacios F., Colonno M. R., Aranake A. C., Campos A., Copeland S. R., Economon T. D., Lonkar A. K., Lukaczyk T. W., Taylor T. W., and Juan J. Alonso. "stanford university unstructured (su2): An open-source integrated computational environment for multi-physics simulation and design". *AIAA Journal, Vol. 287*, 2013. <https://doi.org/10.2514/6.2013-287>.
- [27] Palacios F., Economon T. D., Aranake A. C., Copeland S. R., Lonkar A. K., Lukaczyk T. W., Manosalvas D. E., Naik K. R., Padròn A. S., and Tracey B. et al. "stanford university unstructured (su2): Open-source analysis and design technology for turbulent flows". *AIAA Journal, Vol. 243*, pages 13–17, 2014. <https://doi.org/10.2514/6.2014-0243>.
- [28] Galimberti L., Morelli M., Guardone A., and Zhou B. Y. "propeller noise prediction capabilities within su2". *Proceedings of the AIAA SCITECH 2023 Forum, National Harbor, MD and Online*, page 1548, 2023. <https://doi.org/10.2514/6.2023-1548>.

- [29] Jameson A. "time dependent calculations using multigrid, with applications to unsteady flows past airfoils and wings". *AIAA paper*, Vol. 1596, 1991. <https://doi.org/10.13140/2.1.2459.3608>.
- [30] K. Kundert, G. Sorkin, and A. Sangiovanni-Vincentelli. "applying harmonic balance to almost-periodic circuits". *IEEE Transactions on Microwaves, Theory and Techniques*, 36, page 366–378, 1988. <https://doi.org/10.1109/22.3525>.
- [31] K. Ekici and K.C. Hall. "nonlinear analysis of unsteady flows in multistage turbomachines using harmonic balance,". *AIAA Journal*, 45, page 1047–1057, 2007. <https://doi.org/10.2514/1.22888>.
- [32] Guédéney T., Gomar A., Gallard F., Sicot F., Dufour G., and G. Puigt. "non-uniform time sampling for multiple-frequency harmonic balance computations". *Journal of Computational Physics*, Volume 236, pages 317–345, 1 March 2013. <https://doi.org/10.1016/j.jcp.2012.11.010>.
- [33] Jie Su, Hang Lei, Dai Zhou, Zhaolong Han, Yan Bao, Hongbo Zhu, and Lei Zhou. "aerodynamic noise assessment for a vertical axis wind turbine using improved delayed detached eddy simulation,". *Renewable Energy*, Volume 141, pages 559–569, 2019. <https://doi.org/10.1016/j.renene.2019.04.038>.
- [34] Alex Zanotti and Davide Algarotti. Aerodynamic interaction between tandem overlapping propellers in evtol airplane mode flight condition. *Aerospace Science and Technology*, 124:107518, 2022.
- [35] Savino Alberto, Cocco Alessandro, Zanotti Alex, Tugnoli Matteo, Masarati Pierangelo, and Muscarello Vincenzo. Coupling mid-fidelity aerodynamics and multibody dynamics for the aeroelastic analysis of rotary-wing vehicles. *Energies*, 14(21), 2021.
- [36] Spalart P. and Allmaras S. "a one-equation turbulence model for aerodynamic flows,". *Proceedings of the 30th Aerospace Sciences Meeting and Exhibit, Reno, NV, USA*, page 439, 1994. <https://doi.org/10.2514/6.1992-439>.
- [37] Cakmakcioglu S. C., Bas O., Mura R., and U. Kaynak. "a revised one-equation transitional model for external aerodynamics,". *Proceedings of the AIAA AVIATION 2020 FORUM, virtual event,,* page 2706, 2020. <https://doi.org/10.2514/6.2020-2706>.